Automated parameter selection for accelerated MRI reconstruction via low-rank modeling of local k-space neighborhoods

Efe Ilicak[1,2,*], **Emine Ulku Saritas**[2,3,4], **Tolga Çukur**[2,3,4]

[1] Computer Assisted Clinical Medicine, Mannheim Institute for Intelligent Systems in Medicine, Medical Faculty Mannheim, Heidelberg University, Mannheim, Germany
[2] National Magnetic Resonance Research Center (UMRAM), Bilkent University, Ankara, Turkey
[3] Department of Electrical and Electronics Engineering, Bilkent University, Ankara, Turkey
[4] Neuroscience Program, Bilkent University, Ankara, Turkey

Received 23 September 2021; accepted 1 February 2022

Abstract

Purpose: *Image quality in accelerated MRI rests on careful selection of various reconstruction parameters. A common yet tedious and error-prone practice is to hand-tune each parameter to attain visually appealing reconstructions. Here, we propose a parameter tuning strategy to automate hybrid parallel imaging (PI) – compressed sensing (CS) reconstructions via low-rank modeling of local k-space neighborhoods (LORAKS) supplemented with sparsity regularization in wavelet and total variation (TV) domains.*

Methods: *For low-rank regularization, we leverage a soft-thresholding operation based on singular values for matrix rank selection in LORAKS. For sparsity regularization, we employ Stein's unbiased risk estimate criterion to select the wavelet regularization parameter and local standard deviation of reconstructions to select the TV regularization parameter. Comprehensive demonstrations are presented on a numerical brain phantom and in vivo brain and knee acquisitions. Quantitative assessments are performed via PSNR, SSIM and NMSE metrics.*

Results: *The proposed hybrid PI-CS method improves reconstruction quality compared to PI-only techniques, and it achieves on par image quality to reconstructions with brute-force optimization of reconstruction parameters. These results are prominent across several different datasets and the range of examined acceleration rates.*

Conclusion: *A data-driven parameter tuning strategy to automate hybrid PI-CS reconstructions is presented. The proposed method achieves reliable reconstructions of accelerated multi-coil MRI datasets without the need for exhaustive hand-tuning of reconstruction parameters.*

Keywords: Parallel imaging, Compressed sensing, Regularization, Parameter selection, Self tuning, Low rank

1 Introduction

Magnetic resonance imaging (MRI) offers excellent soft tissue contrast, but it is often hampered by relatively long scan times. Accelerated MRI alleviates this limitation in efficiency by undersampling k-space acquisitions, and then recovering images from undersampled data [1]. Two mainstream approaches for recovery are parallel imaging (PI) that exploits

* Corresponding author: Efe Ilicak, Computer Assisted Clinical Medicine, Mannheim Institute for Intelligent Systems in Medicine, Medical Faculty Mannheim, Heidelberg University, Mannheim, Germany.
E-mail: efe.ilicak@medma.uni-heidelberg.de (E. Ilicak).

Z Med Phys **33** (2023) 203–219
https://doi.org/10.1016/j.zemedi.2022.02.002
www.elsevier.com/locate/zemedi
© 2022 The Author(s). Published by Elsevier GmbH on behalf of DGMP, ÖGMP and SSRMP. This is an open access article under the CC BY-NC-SA license (http://creativecommons.org/licenses/by-nc-sa/3.0/).

the spatial encoding information that modern coil arrays provide [2–6], and compressed sensing (CS) that exploits prior information about image sparsity in known transform domains [7–12]. Recent studies have demonstrated enhanced performance by devising hybrid reconstructions that combine the benefits of receiver arrays and sparsity priors [13–17].

A recent framework for reconstruction from undersampled MR acquisitions is LORAKS (low-rank modeling of local k-space neighborhoods) [1]. LORAKS observes that the system matrix in PI with receiver arrays can be cast as a structured low-rank matrix, and flexibly incorporates additional constraints regarding smoothness of image phase and extent of spatial support [1]. To further improve reconstruction quality, sparsity priors from CS can also be injected into LORAKS by inclusion of regularization terms based on ℓ_1-norm of wavelet coefficients or total variation (TV) norm of image coefficients [18–20]. As such, LORAKS has been successfully demonstrated in a broad range of applications, including multi-contrast imaging [21], fetal imaging [22], and echo-planar imaging [23]. Yet image quality critically depends on the selection of various parameters related to LORAKS (e.g., matrix rank threshold) as well as regularization weights that balance sparsity priors against the physical signal model. In particular, suboptimal parameter selection is known to elicit artifacts or loss of image features [24]. While many studies empirically tune parameters for specific datasets of interest, such exhaustive tuning is computationally challenging and thereby impractical for routine clinical practice [25–27].

Several powerful approaches were previously proposed for tuning of MRI reconstruction parameters. L-curve criterion [28] assumes that the trade-off between data consistency objective governed by the physical signal model and regularization objectives follows an L-shaped curve, and that the optimal parameters can be selected on the point of maximum curvature (i.e., the elbow point). Projection onto epigraph sets [29] determines regularization parameters via geometric projections onto the boundary of convex epigraph sets. Generalized cross-validation [30] first estimates the reconstruction error as a function of regularization terms and regularization weights, and then selects optimal parameters that minimize the estimated error. Similarly, Stein's unbiased risk estimator (SURE) [31] produces online estimates of the expected mean squared error of a reconstruction model [32], and it permits parameter selection via evaluation of estimated error. While existing approaches have been demonstrated for selecting regularization weights in PI [28,32,33] or CS [34–36], remaining reconstruction parameters still require heuristic selections. Therefore, there is a need for a comprehensive approach that automates selection of all relevant parameters in hybrid PI-CS reconstructions.

In this work, we introduce a data-driven parameter tuning strategy to automate hybrid PI-CS reconstructions based on the LORAKS framework, named A-LORAKS-CS. We propose to perform matrix rank selection in LORAKS via singular value soft thresholding. For selection of CS regularization weights, we employ a proven SURE-based method for ℓ_1-norm of wavelet coefficients, and we devise an efficient method based on local standard deviation of reconstructed images for TV-norm of image coefficients. Comprehensive demonstrations are presented on a numerical brain phantom, in vivo balanced steady-state free precession (bSSFP), T_1-weighted, and Time-of-Flight (TOF) acquisitions of the brain, and proton density (PD) weighted acquisitions of the knee. Comparisons are provided against state-of-the-art PI and hybrid PI-CS reconstructions, as well as brute-force methods where parameters are optimized through an exhaustive search by peeking into the fully-sampled ground truth data. The proposed method performs reliably across different imaging contrasts and anatomies. A-LORAKS-CS achieves on par quality to the brute-force hybrid PI-CS reconstructions, while outperforming other competing methods in terms of image quality.

2 Methods

The central aim of this study is to introduce an automated data-driven parameter tuning strategy for reconstruction of multi-coil MRI acquisitions based on the LORAKS framework supplemented with CS sparsity priors. In the following sections, we first introduce the hybrid PI-CS reconstruction formulation, followed by the parameter tuning strategy including the selection of LORAKS parameters, wavelet-domain regularization weight and TV-norm regularization weight.

2.1 Hybrid PI-CS with LORAKS

LORAKS is a powerful approach for reconstructing undersampled MRI acquisitions. LORAKS uses a structured low-rank matrix formulation to harness support, phase and PI constraints [18,37], and it estimates missing k-space data by promoting limited rank in the resulting system matrix [5,21]. The structured system matrix is based on linear shift-invariant interpolation kernels that capture relationships among samples in local k-space neighborhoods. While it is possible to learn these relationships from a fully-sampled central k-space region, it is also possible to generalize LORAKS to calibrationless sampling trajectories [1]. Complementary to LORAKS, CS regularizations can be utilized to improve image quality, by promoting compressibility of data representations in known transform domains. In this work, we utilized two common sparsity priors, namely ℓ_1-norm regularization of wavelet coefficients and total variation (TV) regularization of image coefficients. As such, hybrid PI-CS reconstructions can be cast as a constrained optimization problem:

$$\min_{x} \left(J_r\left(P_S\left(x\right)\right) + \lambda_W \sum_c \left\|\psi\left\{X_c\right\}\right\|_1 + \lambda_{TV} \sum_c \left\|\nabla\left\{X_c\right\}\right\|_1 \right) \quad (1)$$
$$subj.to \quad \mathbb{A}x = x_{acq}$$

The above formulation comprises multiple objectives: a term that enforces low rank in the system matrix, a joint

sparsity term across wavelet coefficients of multi-coil MRI data, and a cumulative sparsity term across TV coefficients of multi-coil MRI data. Meanwhile, strict data consistency is enforced using the constraint in the second line of the equation. In Eq. (1), $J_r(\cdot)$ is a nonconvex penalty function that enforces the matrix rank to be less than or equal to the selected rank estimate r, P_S is the operator that constructs the structured low-rank matrix based on limited spatial support and/or smoothly varying phase from multiple receiver channels (see Appendix A for detailed implementation of these penalty functions and the LORAKS operator). Meanwhile, ψ denotes the wavelet transform operator, λ_W denotes the wavelet regularization weight; ∇ denotes the finite-differences operator and λ_{TV} denotes the TV regularization weight. Lastly, x denotes the k-space data to be estimated (X in image domain) containing all receiver channels, c denotes the index of the receiver channel, x_{acq} are acquired data and $\mathbb{A}$ is the sampling operator.

The reconstruction in Eq. (1) critically depends on the selection of parameters related to LORAKS as well as regularization weights that balance sparsity priors against consistency with the acquired data. There are several parameters of choice in LORAKS that can affect the quality of the structured low-rank recovery problem (see Appendix A for details). The explicit parameters of interest include the matrix rank value r, and the radius of the local k-space neighborhoods (NR). There are also implicit choices such as the support/phase/PI assumptions used during the construction of the LORAKS matrix and the optimization algorithm [1,38]. In this work, we have limited our scope to the selection of r, as well as the selection of wavelet-domain and TV-domain regularization weights λ_W and λ_{TV}.

2.2 A-LORAKS-CS

To automate hybrid PI-CS reconstructions, here we propose an automated parameter selection method based on the LORAKS framework supported with CS sparsity priors, named A-LORAKS-CS. The proposed method addresses the selection of the matrix rank, the wavelet-domain regularization weight, and the TV-domain regularization weight in Eq. (1) in a data-driven manner without requiring manual intervention. Parameter selection is performed sequentially for LORAKS, sparsity and TV projection steps as outlined in Figure 1.

Optimization and stopping criterion

Reconstructions were obtained by solving Eq. (1) using an alternating minimization strategy, with inner splits for LORAKS and CS optimization. In accordance, LORAKS and CS projections were employed in an interleaved fashion with data-consistency projections to produce a quasi-optimal solution at their intersection. A single outer iteration was used [13], and a data-driven stopping criteria was employed to tune the number of inner iterations. The stopping criterion for both LORAKS and CS splits was based on the Euclidean distance between reconstructed images at consecutive iterations. A maximum of 50 inner iterations was prescribed, and optimization for a given split was stopped when the Euclidean norm between two iterations fell below a tolerance of 10^{-3}. The details of the individual projections are described in the following sections.

2.3 Selection of the matrix rank

Here we have limited our scope to a LORAKS implementation based on the S matrix, a structured low-rank matrix with limited spatial support and/or smoothly varying phase assumptions, without virtual conjugate coils. The LORAKS reconstruction was obtained using the multiplicative half-quadratic majorize-minimize algorithm, where the low-rank approximation to S was obtained via a truncated singular value decomposition (SVD) [38]. The matrix approximation problem can be expressed as:

$$\hat{T} = \underset{T:rank(T)=r}{\operatorname{argmin}} \|S - T\|_F^2 \tag{2}$$

Here, T is the low-rank approximation to S, and $\|\cdot\|_F$ denotes the Frobenius norm of a matrix. Assume that the SVD of the structured matrix is given as $S = U\Sigma V^H$, where Σ is diagonal and U, V are orthonormal matrices. The low-rank approximation is then:

$$\hat{T} = U\Sigma_{\leq r,\leq r}V^H \tag{3}$$

where $\Sigma_{\leq r,\leq r}$ denotes that all entries in Σ except the ones with row and column indices smaller than or equal to r have been replaced with zeros (i.e., all singular values excluding the highest r values have been replaced with zeros). Noting that $U^HU = I$, the linear operator that performs the truncation can be expressed as:

$$\hat{T} = \left(UI_{\leq r,\leq r}U^H\right)\left(U\Sigma V^H\right) = \left(UI_{\leq r,\leq r}U^H\right)S \tag{4}$$

It can be observed that $UI_{\leq r,\leq r}U^H$ is Hermitian symmetric [38].

To select the matrix rank (r), we devised a SURE-based approach in this study. SURE is a data-driven method for calculating mean squared error (MSE) in estimating a true signal from measurements corrupted by additive Gaussian noise [31]. Let $y \in \mathbb{C}^m$ be the true complex signal, $\eta \in \mathbb{C}^m$ be additive zero-mean complex Gaussian noise with standard deviation σ for both the real and imaginary components, and $x_{acq} = y + \eta$ be the acquired complex data. The SURE expression for a linear denoiser can be derived as [33]:

$$\mathbb{E}\left\{\left\|P_\theta\left(x_{acq}\right) - y\right\|_2^2\right\} = \mathbb{E}\left\{SURE_{P_\theta}\left(x_{acq}\right)\right\} \tag{5}$$

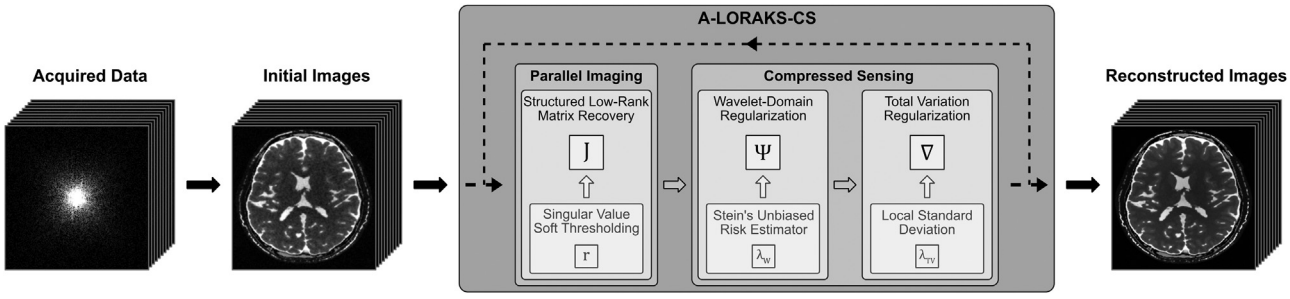

Figure 1. Flowchart of A-LORAKS-CS, a data-driven parameter tuning strategy to automate hybrid PI-CS reconstructions. A-LORAKS-CS utilizes the LORAKS framework as its PI component, and wavelet- and TV-domain regularization as its CS component. Parameter selection for PI and CS components are performed sequentially and independently. Matrix rank in LORAKS is selected with singular value soft thresholding. Threshold for wavelet coefficients in sparsity projections is selected according to Stein's unbiased risk estimate. Threshold for finite-differences coefficients in TV projections is selected according to local standard deviation estimates. Collectively, A-LORAKS-CS achieves robust, data-driven reconstructions from undersampled acquisitions without requiring manual intervention.

$$SURE_{P_\theta}\left(x_{acq}\right) = -m\sigma^2 + \left\| P_\theta\left(x_{acq}\right) - x_{acq}\right\|_2^2 + 2\sigma^2 trace\left(P_\theta\left(x_{acq}\right)\right) \quad (6)$$

where P_θ is the operator characterizing the linear denoiser with parameters θ. If P_θ is Hermitian symmetric, Eq. (6) can equivalently be implemented by partitioning the complex vector space for data into real and imaginary parts [33]. Because the above expression depends on the acquired data and not on the ground truth signal, expected MSE of the estimator can be calculated without supervision. In turn, an optimal set of parameters can be selected to minimize the expected MSE. Note that LORAKS can be viewed as a linear denoiser that performs low-rank matrix approximation to remove undesirable signals in the measured data including noise. Thus, taking P_θ as the LORAKS operator with $\theta = (r, NR)$, here we propose to select r based on the SURE expression in Eq. (6). Yet, explicit calculation of low-rank matrix approximations for each possible value in a range for r would be computationally exhaustive. In this study, we instead reparametrize the low-rank problem as a soft-thresholding operation on singular values:

$$\hat{T} = U\Sigma_{\leq r, \leq r}V^H \approx UM\Sigma V^H, \quad where \quad M_{i,j} = \begin{cases} \dfrac{S_{shrink}\left(\varepsilon_i\right)}{\varepsilon_i}, & i = j \\ 0, & i \neq j \end{cases} \quad S_{shrink}(\varepsilon_i) = \frac{\varepsilon_i}{|\varepsilon_i|}\max\left(0, |\varepsilon_i| - \lambda_\varepsilon\right) \quad (7)$$

where ε_i is the ith singular value, $S_{shrink}(\cdot)$ is the soft-thresholding operation, and λ_ε is the threshold to be selected for singular values. Theory suggests that this reparametrization allows selection of an optimal threshold for the singular values of a matrix based on SURE in the absence of structured noise [39], and a recent study on ESPIRiT demonstrated derivation of pseudo-optimal thresholds paralleling results from exhaustive search in cases with structured noise [33]. Inspired by these studies, here we propose to determine the matrix rank in LORAKS via soft-thresholding of the singular values in S. Accordingly, the pseudo-optimal value for λ_ε is obtained via a SURE expression.

$$\hat{\lambda_\varepsilon} \approx \underset{\lambda_\varepsilon}{\text{argmin}} \quad SURE_{\lambda_\varepsilon}\left(x_{acq}\right) \quad (8)$$

To determine the matrix rank for LORAKS, the rank of the soft-thresholded matrix can then be identified as $r = \sum_i \varphi(\varepsilon_i - \hat{\lambda_\varepsilon})$, where φ is the binary step function.

Unlike the selection of the matrix rank, the choice of NR is nontrivial since larger NR is associated with increased memory requirements. In theory [1,5], higher values of NR increase reconstruction performance, although the performance curve with respect to NR might be non-monotonic. Here, we selected $NR = 3$ based on the trade-off between the reconstructed image quality and the available memory of the system on which the experiments were conducted (see Supp. Figure 1).

2.4 Selection of the wavelet-domain regularization weight

Sparsity projections were implemented to reduce residual artifacts in the reconstructions. The projections were implemented to solve the following minimization problem:

$$SP\left(\bar{X}\right) = \underset{X}{arg\,\min}\|\bar{x} - EX\|_2^2 + \lambda_W\|\psi\{X\}\|_1 \quad (9)$$

where $E = \mathbb{A}F$ is the encoding matrix that also involves the Fourier operator with the sampling operator, $\bar{x}$ denote the input to the projection in k-space. A common approach to solve the

optimization in Eq. (9) is iterative soft-thresholding (IST) that shrinks wavelet coefficients [7,40]:

$$X^{(i)} = \psi^{-1} S_{shrink}\left(\psi\left\{X^{(i-1)} + E^H\left(\bar{x} - EX^{(i-1)}\right)\right\}\right)$$
$$S_{shrink}\left(u_j\right) = \frac{u_j}{|u_j|}\max\left(0, |u_j| - \lambda_W\right) \tag{10}$$

where u_j denote individual wavelet coefficients. To improve convergence speed of IST, here we adopted the optimization approach introduced by Khare et al. [34] that uses reconstructions at two prior iterations to compute the updated reconstruction. Accordingly, the reconstruction at the *i*th iteration was expressed as:

$$X^{(i)} = \psi^{-1} S_{shrink}\left(\psi\left\{h^{(i)}\right\}\right)$$
$$h^{(i)} = g^{(i-1)} + E^H\left(\bar{x} - Eg^{(i-1)}\right) \tag{11}$$
$$g^{(i-1)} = \left(1 + \frac{i-1}{i+2}\right)X^{(i-1)} - \frac{i-1}{i+2}X^{(i-2)}$$

where $g^{(i-1)}$ denotes a linear combination of reconstructions from the two prior iterations, the combination weights are set according to Nesterov's optimal gradient scheme, and $h^{(i)}$ is an intermediate image derived from $g^{(i-1)}$ by enforcing consistency to acquired k-space samples.

At each iteration, λ_W was selected based on the SURE criterion for minimizing ℓ_2-norm error between the intermediate image $h^{(i)}$, and its soft-thresholded version $X^{(i)}$ [31,34,35]:

$$\lambda_W = \underset{\lambda_W}{\operatorname{argmin}} \; SURE_{\lambda_W}\left(h^{(i)}\right) \tag{12}$$

To identify the optimal threshold, a line-search was used with the range initialized to $[10^{-4}\ 10^{-2}]$. During the course of reconstruction, the search range was adaptively adjusted to obtain finer resolution around the settled minima. Here we generalized the method introduced by Khare et al. [34] to multiple receiver channel settings. The regularization weight was first selected independently for each coil element. Optimal values for individual coils were averaged, and the resulting weight was used for joint-sparsity regularization across all coils.

2.5 Selection of the TV-domain regularization weight

TV projections were employed to reduce aliasing interference and noise in the reconstructions. The projections were implemented by minimizing the following objective:

$$TV\left(\bar{X}\right) = \underset{X}{\operatorname{argmin}}\left\|\bar{X} - X\right\|_2^2 + \lambda_{TV}\left\|\nabla\{X\}\right\|_1 \tag{13}$$

where $\bar{X}$ denotes the input to the TV projection in image domain. A fast iterative clipping algorithm with parameters adopted from [41] was used for solving this optimization problem:

$$X^{(i)} = \bar{X} - \nabla^t\left\{z^{(i-1)}\right\}$$
$$z^{(i)} = S_{clip}\left(z^{(i-1)} + \nabla\left\{X^{(i)}\right\}/\alpha\right) \tag{14}$$

where ∇^t denotes the adjoint finite-differences operator, $X^{(i)}$ denotes the reconstructed image at *i*th iteration of the splitting algorithm, α is the update rate parameter, $z^{(i)}$ denotes the auxiliary vector in the finite-differences domain and $z^{(0)} = 0$. The clipping function that serves to penalize finite-differences coefficients below a specific threshold was taken as:

$$S_{clip}\left(z_j\right) = \begin{cases} z_j, & |z_j| < \frac{\lambda_{TV}}{2} \\ \left(\frac{\lambda_{TV}}{2}\right)\cdot\exp\left(j\angle z_j\right), & otherwise \end{cases} \tag{15}$$

where z_j denote individual finite-differences coefficients. At each iteration, λ_{TV} was selected via a non-iterative procedure that uses edge maps derived from reconstructions at the previous iteration. Edge maps were constructed by emphasizing high-frequency signals in MR images as inspired by Guo and Huang [42]. Note that high-frequency signals carry contributions from not only edge structures near tissue boundaries but also from white Gaussian noise. To minimize formation of artefactual edges due to noise amplification, images were smoothed with a Gaussian kernel of $\sigma = 2$ and size set to 3σ along each axis to cover 99% of the variability in the kernel. Our analyses indicated that the choice of σ that controls the degree of spatial smoothing does not have a notable influence on the final reconstruction performance (see Supp. Figure 2 for representative results). Thus, we selected an intermediate value that offered decent noise suppression without over-smoothing the images visually. A spatial map that reflects energy levels associated with edge structure was then computed as the square-root of the local standard deviations (*LSD*) to emphasize high-frequency information:

$$Q = \sqrt{LSD(\dot{X})} \tag{16}$$

Here, Q represents the edge map, *LSD* represents the local standard deviation operation, $\dot{X}$ represents the smoothed image. To increase sensitivity for compact edges due to rapid transition between neighboring pixels, *LSD* was measured across a 3×3 neighborhood. It is expected that pixels with reliable edge features will have high values in Q, whereas remaining pixels will have notably lower values. Therefore,

λ_{TV} was selected as the fraction of the median intensity in edge maps [36]:

$$\lambda_{TV} = median\,(Q)\,/\gamma \tag{17}$$

The fraction constant in the above equation was selected as $\gamma = 10$, as this value worked reliably across various datasets, and overall reconstruction performance showed minimal sensitivity to the selection (see Supp. Figure 3 for representative results).

2.6 Alternative reconstructions

For each dataset, several alternative reconstructions were computed to comparatively demonstrate the proposed A-LORAKS-CS approach.

A-ESPIRiT: An ESPIRiT reconstruction was performed with SURE-based automatic parameter selection [33]. Kernel size, eigenvalue threshold and size of the signal subspace were selected from the auto-calibration region based on the SURE criterion. To mitigate excessive computational burden, kernel size and eigenvalue threshold were determined for a single central cross-section within each volume and were assigned to the remaining cross-sections, whereas the size of the signal subspace was computed separately for each cross-section.

A-LORAKS: Automated LORAKS projections were performed as described in the PI component of the proposed method, but CS projections were omitted during reconstruction.

PESCaT: A hybrid PI-CS reconstruction was implemented using a geometric projection onto epigraph sets (PES) technique [29]. This method uses heuristically determined SPIRiT projections [4] with fixed parameters, and a PES approach to determine regularization weights for wavelet-domain and TV-domain coefficients.

BF-LORAKS and BF-LORAKS-CS: Two brute-force reconstructions were implemented to obtain a target level of image quality for LORAKS-type reconstructions. The first one was BF-LORAKS that performed an exhaustive optimization of the matrix rank value (r) to obtain a PI-only reconstruction. The optimization of r was performed by searching across 20 possible values, ranging between 5% and 100% of the largest singular value. The second one was BF-LORAKS-CS that leveraged BF-LORAKS for PI projections, and exhaustively optimized regularization weights λ_W and λ_{TV} for the CS projections. The optimization of regularization weights were performed by searching across 100 possible combinations of wavelet-domain and TV-domain regularization weights [26]. For both reconstructions, exhaustive optimization of reconstruction parameters assumed the availability of fully-sampled ground truth images. Optimal parameter sets were observed to be consistent across separate cross-sections within a given volume for individual subjects. Thus, for computational efficiency, brute-force searches were conducted in a central cross section, and reconstruction parameters that yielded near-optimal quantitative performance metrics were assigned to the remaining cross-sections within each subject.

Reconstructions were performed separately on individual cross-sections of three-dimensional (3D) volumes. To do this, 3D k-space acquisitions were Fourier transformed across the fully-sampled readout dimension, and then split along that dimension to select single cross sections. Thus, 2D LORAKS operators were used in A-LORAKS, A-LORAKS-CS, BF-LORAKS and BF-LORAKS-CS; 2D interpolation kernels were used in PESCaT; and 2D sensitivity maps were used in A-ESPIRiT. For all methods, reconstructions were allowed a maximum of 50 iterations, with identical stopping criteria to A-LORAKS-CS. Reconstructed images (coil- and/or multiple-acquisitions) were combined with sum-of-squares. All reconstruction algorithms were implemented in MATLAB (MathWorks, MA) on a PC with 16 GB memory. Upon publication, codes will be openly available for general use at https://github.com/icon-lab/mrirecon.

2.7 Undersampling patterns

Variable-density random sampling patterns were used to retrospectively undersample fully-sampled acquisitions [43]. Sampling patterns were generated based on a polynomial density function to achieve 2D isotropic acceleration in two phase-encode dimensions. For additional analyses, separate sampling patterns were generated for 1D acceleration in a single phase-encode dimension. Although LORAKS supports sampling patterns without dedicated auto-calibration regions (see Supp. Figure 4), for a fair comparison among competing methods some of which were autocalibrating, central k-space was fully-sampled up to 10% of maximum spatial frequency in each dimension. For a given sampling density, 1000 candidate patterns were pseudo-randomly generated. The candidate that minimized the aliasing energy was then selected [11].

2.8 Numerical phantom experiments

Simulations were performed on a realistic brain phantom at 0.5 mm isotropic resolution (http://brainweb.bic.mni.mcgill.ca/brainweb). Phase-cycled bSSFP images were calculated as described in [40], with $N = 4$ phase-cycling values ($\Delta\phi$) spanning $[0, 2\pi)$ in equi-spaced intervals. Bivariate Gaussian noise was added to phase-cycled bSSFP images to attain acquisition SNR = 30 for cerebrospinal fluid (CSF). 3D acquisitions that cover the brain in the superior-inferior direction were obtained for 10 axial cross-sections using a flip angle of 45° and TR/TE of 5.0/2.5 ms with 8 receiver channels organized in a circularly symmetric geometry (see Supp. Figure 5 for banding-free bSSFP images in a central cross-section). Data were 2D undersampled at $R = 2, 3, 4, 6$ in two phase-encode dimensions, and 1D undersampled at $R = 2, 3, 4$ in a single phase-encode dimension.

Reconstruction quality was assessed via quantitative metrics measured on combined bSSFP images. For a given cross-section, the reference image was designated as the reconstruction obtained from fully-sampled acquisitions combined across both the coils and phase cycles. Peak signal-to-noise ratio (PSNR), structural similarity index (SSIM), and normalized mean-squared error (NMSE) metrics were measured between the reconstructed image and the reference image, while excluding background regions (i.e., air). To prevent bias due to intensity differences, 98% of pixel intensities were normalized to the range [0 1].

2.9 In vivo experiments

To demonstrate the proposed method in vivo, experiments were conducted on fully-sampled phase-cycled bSSFP, T_1-weighted, and TOF acquisitions of the brain, as well as PD-weighted fast spin echo (FSE) knee acquisitions. The brain datasets were acquired using a 3T scanner (Magnetom Trio, Siemens, Erlangen, Germany) with 3D sequences and a 12-channel head coil. Five healthy subjects were scanned under each protocol. All participants gave written informed consent, and the imaging protocols were approved by the local ethics committee. The fully-sampled human knee experiments were conducted on a public dataset [44]. The knee images were acquired on a 3T scanner (Discovery MR 750, GE Healthcare, Milwaukee, USA) with a PD-weighted 3D sequence and an 8-channel knee coil.

The bSSFP protocol comprised a flip angle of 30°, a TR/TE of 8.08/4.04 ms, a field-of-view (FOV) of 218 mm × 218 mm, an isotropic resolution of 0.85 mm, a matrix size of 256 × 256 × 96, and $N = 4$ separate acquisitions with phase-cycling values ($\Delta\phi$) spanning $[0, 2\pi)$ in equispaced interval. The T_1-weighted protocol comprised a flip angle of 9°, a TR/TE of 2300/2.98 ms, a FOV of 256 mm × 240 mm, a resolution of $1.0 \times 1.0 \times 1.2\,mm^3$, and a matrix size of 256 × 240 × 160. The TOF protocol comprised a flip angle of 18°, a TR/TE of 38/3.19 ms, a FOV of 204 mm × 204 mm, an isotropic resolution of 0.8 mm, and a matrix size 256 × 256 × 75. The knee protocol comprised a TR/TE of 1550/25 ms, 40 ms echo train length, a FOV of 160 mm × 160 mm, a resolution of $0.5 \times 0.5 \times 0.6\,mm^3$, and a matrix size of 320 × 320 × 256. The bSSFP and TOF acquisitions were hardware compressed from 12 receiver channels into 4 channels during acquisition. For individual acquisitions in each subject, 10 central cross-sections were extracted for reconstruction experiments. Data were retrospectively undersampled via variable-density undersampling in the phase-encode dimensions. Undersampling was performed to achieve 2D acceleration at $R = 2$, 3, 4 for all acquisitions, and additionally at $R = 6$ for T_1-weighted acquisitions. Separate analyses were performed to achieve 1D acceleration at $R = 2$, 3, 4 for T_1-weighted acquisitions.

To evaluate reconstruction performance, PSNR, SSIM and NMSE metrics were calculated across individual cross-sections. To prevent bias due to intensity differences, 98% of pixel intensities were normalized to the range [0 1]. Measurements were only performed over image regions containing tissue signals while excluding background regions. Binary foreground/background masks were extracted semi-automatically using a region-growing algorithm with manually specified seeds [45]. For in vivo bSSFP data, the reference image was selected as the coil and phase-cycle combined fully-sampled acquisitions to suppress banding artifacts. For the remaining datasets, the reference images were selected as the coil combined fully-sampled acquisitions.

3 Results

3.1 Numerical phantom experiments

The proposed method was first demonstrated on bSSFP acquisitions of a numerical phantom across 2D acceleration factors $R = 2$–6. Figure 2 displays representative reconstructions at $R = 4$ obtained with A-ESPIRiT, A-LORAKS, PESCaT, A-LORAKS-CS, as well as brute-force optimized BF-LORAKS and BF-LORAKS-CS. A-ESPIRiT displays elevated error levels broadly across the reconstructed image. A-LORAKS yields visibly lower artifacts compared to A-ESPIRiT, yet residual errors remain. The addition of CS priors improves image quality, and PESCaT and A-LORAKS-CS achieve visibly reduced reconstruction error compared to PI-only reconstructions. Furthermore, A-LORAKS-CS maintains similar error performance to brute-force based BF-LORAKS-CS, without access to the fully-sampled reference image for parameter selection.

Quantitative assessments of reconstruction performance are listed in Table 1 for 2D acceleration, and in Supp. Table 1 for 1D acceleration. Note that brute-force methods designate a target for reconstruction performance as their parameter selection is guided by access to the fully-sampled data. We observe that CS priors significantly improve reconstruction quality and the hybrid PI-CS approaches outperform the PI-only reconstructions. Among the hybrid PI-CS methods, A-LORAKS-CS achieves the highest reconstruction quality, performing competitively with the brute-force method. On average across R for 2D acceleration, A-LORAKS improves (PSNR, SSIM, NMSE) by (3.34 dB, 8.45%, 1.51×10^{-2}) over A-ESPIRiT; and A-LORAKS-CS outperforms PESCaT by (1.90 dB, 3.47%, 0.37×10^{-2}). For 1D acceleration, A-LORAKS improves (PSNR, SSIM, NMSE) by (5.69 dB, 14.70%, 4.32×10^{-2}) over A-ESPIRiT; and A-LORAKS-CS outperforms PESCaT by (2.03 dB, 5.17%, 0.59×10^{-2}). Taken together, these results suggest that A-LORAKS-CS can perform near-optimal parameter selection for the reconstruction of undersampled acquisitions across various acceleration rates.

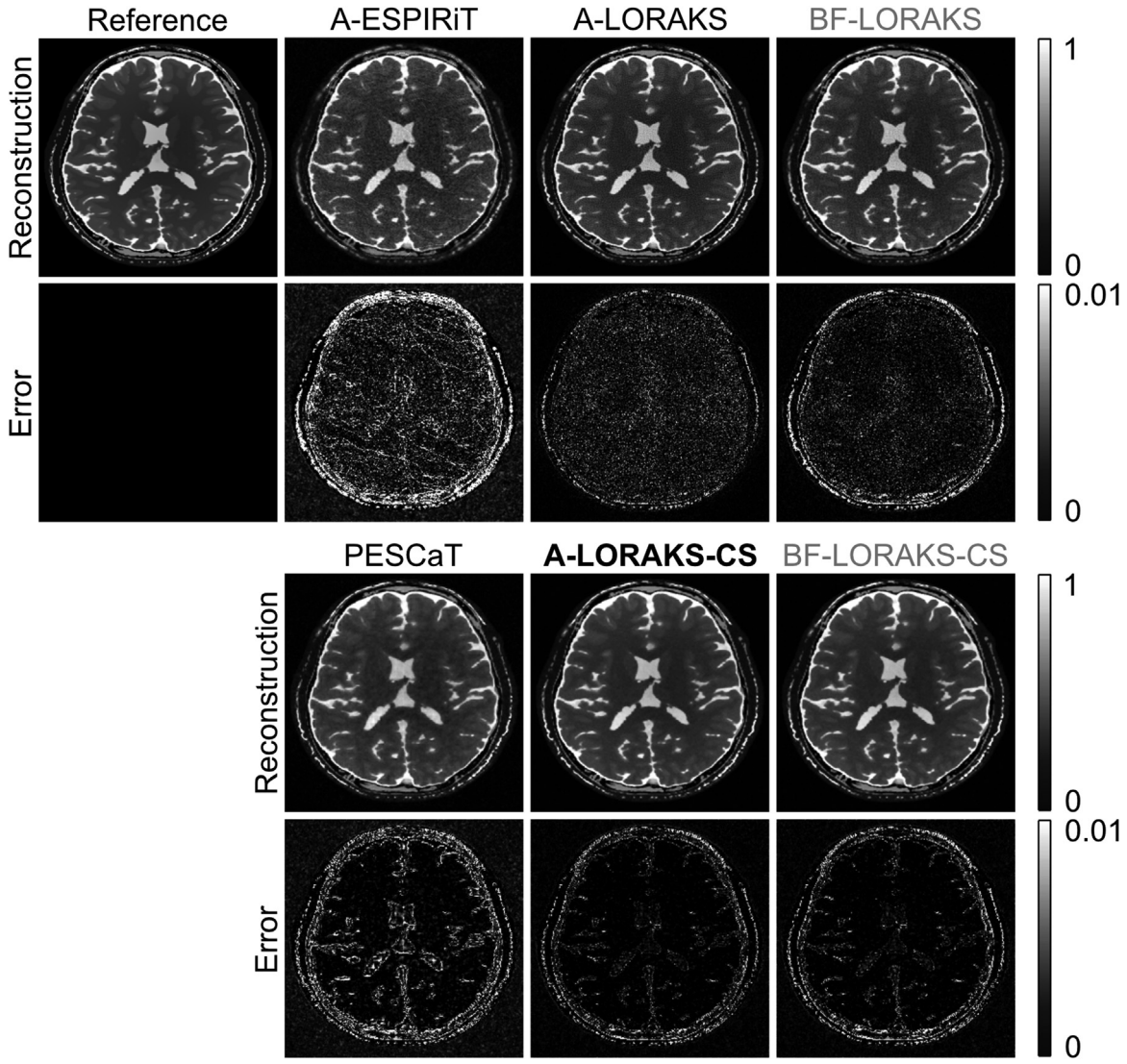

Figure 2. Phase-cycled bSSFP reconstructions of the numerical phantom obtained at $R = 4$ are shown for competing reconstruction methods. In addition, squared error maps with respect to the fully-sampled reference image are displayed. The proposed A-LORAKS-CS method yields visibly reduced reconstruction errors compared to the competing methods, while offering similar reconstruction quality to the brute-force based hybrid PI-CS technique BF-LORAKS-CS without having access to the fully-sampled reference image. Here, the brute-force methods (marked in gray font) have access to the fully-sampled data, and are presented only to provide a target level for the image quality.

3.2 In vivo experiments

Next, we demonstrated A-LORAKS-CS on in vivo bSSFP, T_1-weighted, and TOF acquisitions in the brain and FSE acquisitions in the knee. Representative reconstructions for 2D undersampled acquisitions are displayed in Figures 3–6. As depicted in Figure 3, A-ESPIRiT reconstruction of bSSFP images manifests residual artifacts across tissues and near tissue boundaries, which are mostly alleviated by A-LORAKS. In addition, inclusion of CS priors with A-LORAKS-CS further improves artifact suppression and yields higher image quality.

In Figure 4, representative reconstructions for T_1-weighted acquisitions are displayed at $R = 4$ for two representative subjects (see Supp. Figure 6 for respective squared error maps). Here, while A-ESPIRiT and A-LORAKS maintain relatively similar error performances, these reconstructions show broadly distributed residual errors. In contrast, PESCaT and A-LORAKS-CS further dampen reconstruction errors by utilizing both PI and CS priors.

In Figure 5, a representative cross-section as well as maximum-intensity-projections (MIPs) obtained across the volume are shown for the competing methods for TOF acquisitions at $R = 4$. The artifacts arising from residual errors are

Table 1
Quality of numerical phantom reconstructions assessed via PSNR, SSIM and NMSE. Measurements are reported separately for each method as mean ± std across cross-sections. Bold font marks the top performing reconstructions apart from the brute-force methods (marked in italics font).

PSNR (dB)

Acceleration	A-ESPIRiT	A-LORAKS	*BF-LORAKS*	PESCaT	**A-LORAKS-CS**	*BF-LORAKS-CS*
$R=2$	29.60 ± 0.14	30.89 ± 0.34	*31.18 ± 0.26*	31.22 ± 0.16	**33.08 ± 0.37**	*32.95 ± 0.43*
$R=3$	23.31 ± 0.19	29.51 ± 0.17	*30.00 ± 0.23*	29.82 ± 0.12	**32.51 ± 0.18**	*32.15 ± 0.14*
$R=4$	23.85 ± 0.17	28.56 ± 0.13	*28.01 ± 0.20*	28.22 ± 0.10	**30.96 ± 0.10**	*30.30 ± 0.16*
$R=6$	21.86 ± 0.24	26.35 ± 0.13	*26.30 ± 0.16*	25.38 ± 0.23	**27.59 ± 0.26**	*27.79 ± 0.29*

SSIM (%)

Acceleration	A-ESPIRiT	A-LORAKS	*BF-LORAKS*	PESCaT	**A-LORAKS-CS**	*BF-LORAKS-CS*
$R=2$	78.67 ± 0.38	86.94 ± 0.31	*89.45 ± 0.24*	94.09 ± 0.07	**95.97 ± 0.12**	*95.84 ± 0.10*
$R=3$	60.08 ± 0.38	78.75 ± 0.34	*84.03 ± 0.26*	92.01 ± 0.09	**95.85 ± 0.10**	*95.72 ± 0.09*
$R=4$	71.00 ± 0.26	77.02 ± 0.22	*82.73 ± 0.32*	90.57 ± 0.26	**95.47 ± 0.08**	*95.01 ± 0.12*
$R=6$	64.46 ± 0.35	73.74 ± 0.26	*74.43 ± 0.36*	86.41 ± 0.43	**93.14 ± 0.18**	*93.40 ± 0.21*

NMSE (10^{-2})

Acceleration	A-ESPIRiT	A-LORAKS	*BF-LORAKS*	PESCaT	**A-LORAKS-CS**	*BF-LORAKS-CS*
$R=2$	0.77 ± 0.02	0.57 ± 0.04	*0.54 ± 0.03*	0.53 ± 0.02	**0.35 ± 0.03**	*0.36 ± 0.03*
$R=3$	3.28 ± 0.12	0.79 ± 0.02	*0.70 ± 0.03*	0.73 ± 0.02	**0.39 ± 0.02**	*0.43 ± 0.01*
$R=4$	2.90 ± 0.08	0.98 ± 0.02	*1.11 ± 0.04*	1.06 ± 0.01	**0.56 ± 0.01**	*0.66 ± 0.02*
$R=6$	4.59 ± 0.19	1.63 ± 0.04	*1.65 ± 0.04*	2.04 ± 0.09	**1.22 ± 0.06**	*1.17 ± 0.07*

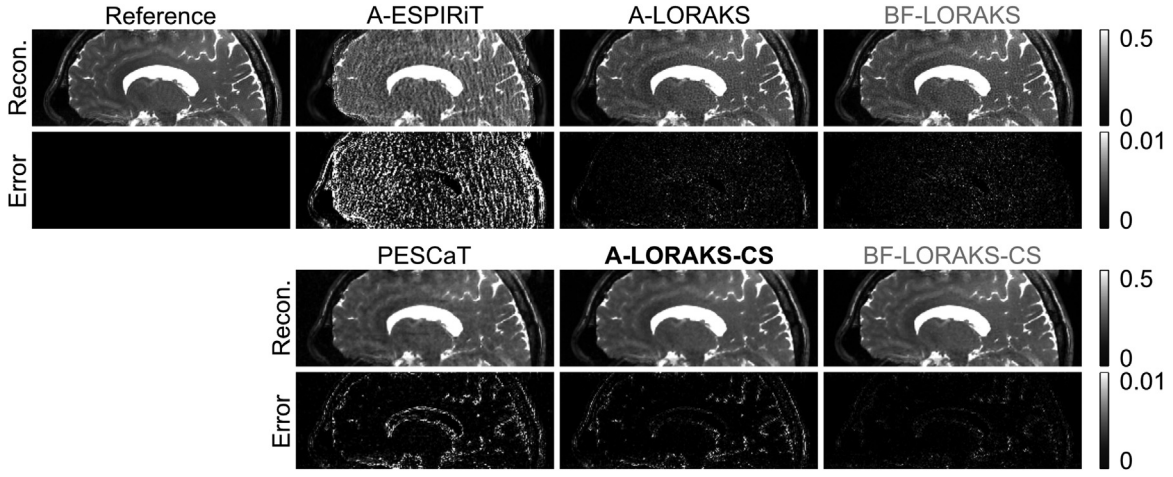

Figure 3. In vivo bSSFP acquisitions of the brain were reconstructed at $R=4$. Reconstructions from a representative cross-section and respective squared error maps with respect to the fully-sampled reference image are displayed for the competing methods. A-ESPIRiT suffers from residual artifacts across tissues and boundaries. A-LORAKS significantly dampens the error and performs similarly to the PI-only brute-force reconstruction BF-LORAKS. Meanwhile the proposed A-LORAKS-CS approach further dampens broadly distributed residual artifacts and offers the closest performance to the hybrid brute-force reconstruction BF-LORAKS-CS.

apparent in the MIPs of A-ESPIRiT and A-LORAKS, whereas the MIP of PESCaT suffers from inconsistencies between different cross-sections. Meanwhile, A-LORAKS-CS yields enhanced artifact suppression and image quality.

In Figure 6, representative reconstructions of knee acquisitions are displayed at $R=3$. Here we observe that the A-ESPIRiT approach suffers from losses at tissue boundaries in regions with low signal intensity due to erroneous estimation of respective eigenvalue thresholds, whereas A-LORAKS better alleviates these artifacts. Nevertheless, both methods have residual reconstruction errors. In contrast, with the added CS priors PESCaT and A-LORAKS-CS yield improved image

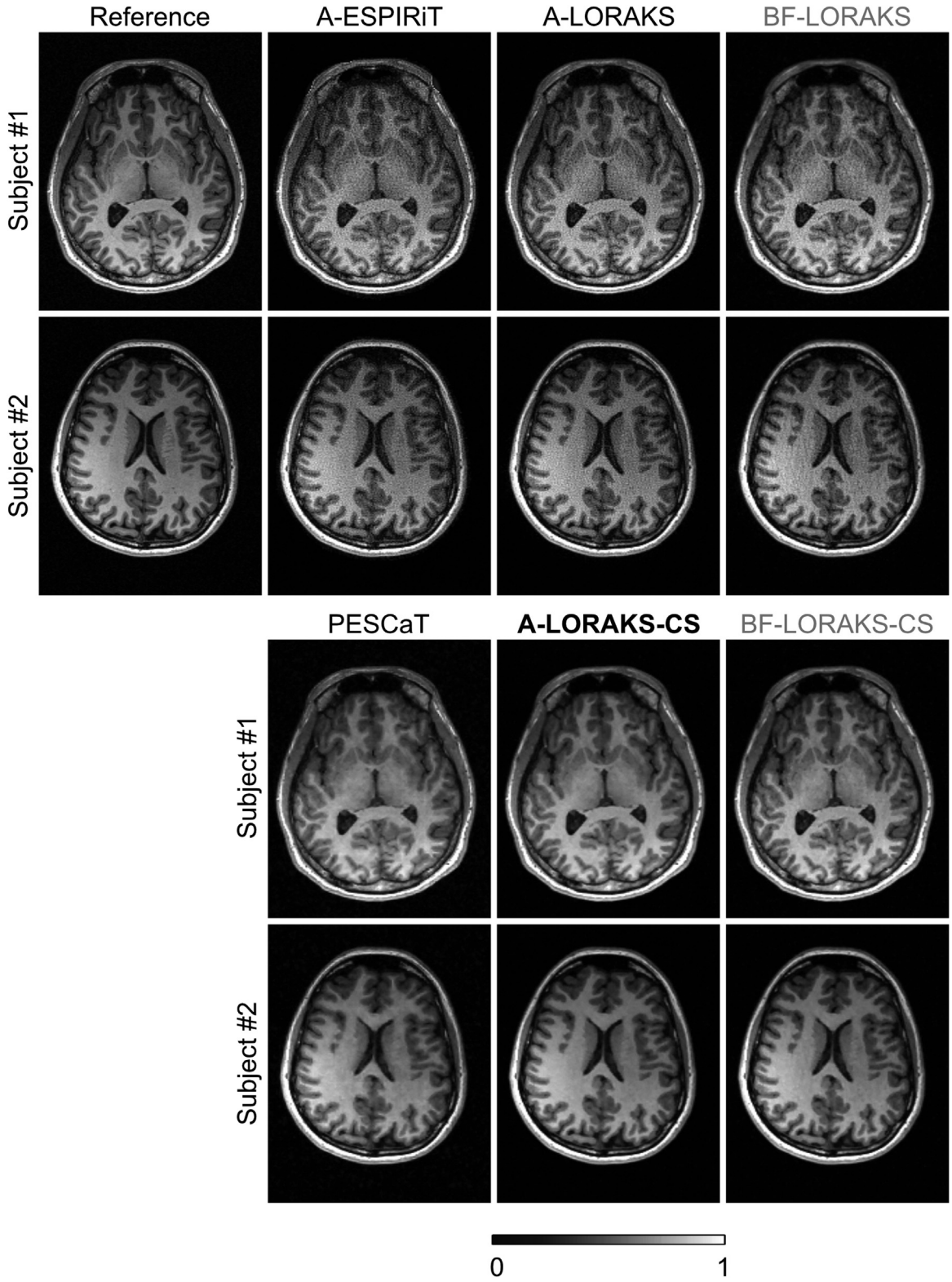

Figure 4. In vivo T_1-weighted acquisitions of the brain were reconstructed at $R = 4$. Reconstructions from representative cross-section from two subjects are displayed for the competing methods. CS regularization noticeably improves reconstruction quality for all examined methods, and overall A-LORAKS-CS achieves on par performance with the hybrid PI-CS brute-force reconstruction BF-LORAKS-CS.

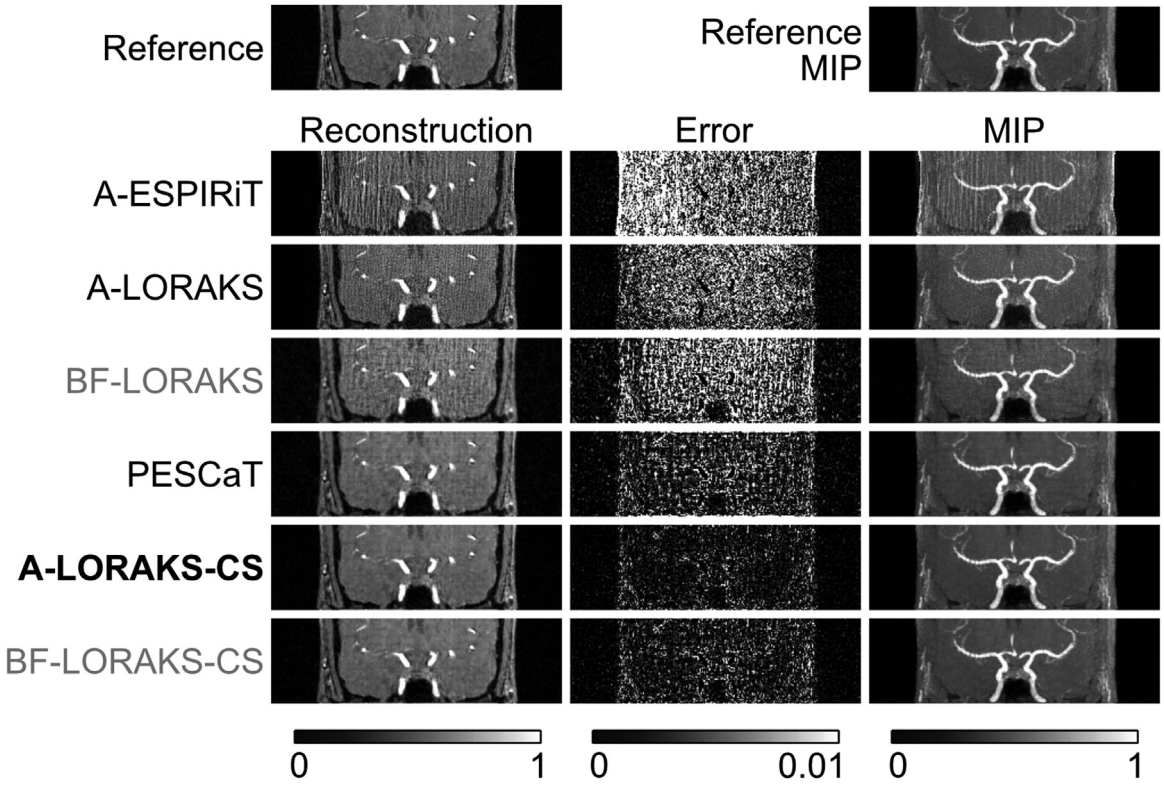

Figure 5. In vivo TOF acquisitions of the brain were reconstructed at $R = 4$. The results are displayed for a representative cross-section along with the error maps and maximum-intensity projections (MIPs) obtained across the volume. A-ESPIRiT suffers from broad errors across the FOV. A-LORAKS improves suppression of aliasing artifacts, yet some reconstruction errors remain. PESCaT suffers from inconsistencies between different cross-sections that create artifacts in the MIP image. In contrast, A-LORAKS-CS yields noticeably improved reconstruction quality for both the cross-section and the MIP.

quality. In particular, A-LORAKS-CS achieves the highest quality overall, with similar image quality and error performance compared to the brute-force reconstruction.

Visual observations regarding the performance of A-LORAKS-CS are also supported by quantitative assessments listed in Tables 2–5 for 2D acceleration, and in Supp. Table 2 for 1D acceleration. At each R, A-LORAKS-CS yields higher PSNR, SSIM and NMSE scores compared to A-ESPIRiT and A-LORAKS (except for PSNR and NMSE at $R = 2$ in bSSFP), while performing similarly to brute-force based BF-LORAKS-CS. Likewise, A-LORAKS-CS yields higher PSNR, SSIM and NMSE compared to PES-based hybrid PI-CS reconstruction PESCaT (except for PSNR and NMSE at $R = 2$ in FSE). For 2D acceleration, A-LORAKS-CS improves (PSNR, SSIM, NMSE) over PESCaT on average by (2.74 dB, 3.74%, 0.39×10^{-2}) in bSSFP acquisitions; by (0.83 dB, 1.73%, 0.18×10^{-2}) in T_1-weighted acquisitions; by (2.48 dB, 7.30%, 0.73×10^{-2}) in TOF acquisitions; and by (0.10 dB, 0.72%, 0.02×10^{-2}) in FSE acquisitions. For 1D acceleration, A-LORAKS-CS outperforms PESCaT by (1.45 dB, 3.83%, 0.60×10^{-2}) in reconstruction of T_1-weighted acquisitions.

Overall, A-LORAKS-CS consistently outperforms PI-only reconstructions, as well as the hybrid PESCaT method. Sample reconstruction times for competing methods are listed in Supp. Table 3 for a single cross-section. Among automated parameter selection approaches, A-LORAKS-CS has on par run time with A-ESPIRiT, albeit relatively longer run time compared to A-LORAKS and PESCaT. Note that, in return for this increase in computational load, A-LORAKS-CS achieves the highest reconstruction quality among competing methods (except for two cases: PSNR and NMSE at $R = 2$ for bSSFP, and at $R = 2$ for FSE acquisitions). Importantly, A-LORAKS-CS has nearly an order-of-magnitude shorter run time compared to BF-LORAKS-CS, which performs parameter selection via exhaustive search over candidate values. At the same time, it maintains the closest performance to BF-LORAKS-CS across different sequences and acceleration rates. Taken together, these results demonstrate the performance improvements obtained with the proposed approach

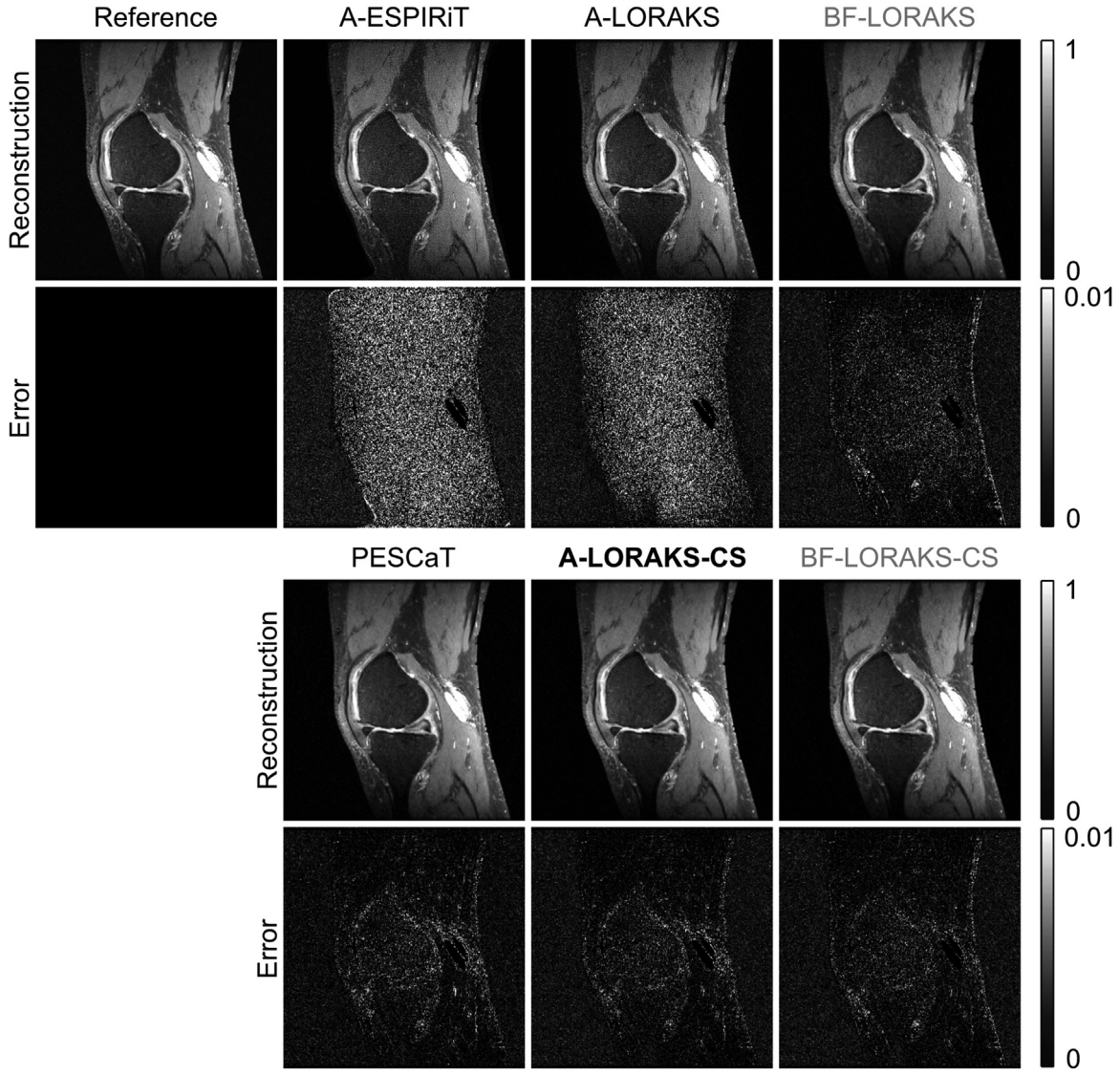

Figure 6. In vivo FSE acquisitions of the knee were reconstructed at $R = 3$. A-ESPIRiT suffers from losses at tissue boundaries in regions with low signal intensity, whereas A-LORAKS does not suffer from these artifacts. Nevertheless, both methods suffer from distributed reconstruction errors across the FOV. The CS priors improve the reconstruction performance and better suppress aliasing artifacts. Overall, A-LORAKS-CS maintains the closest image quality to the brute-force reconstructions.

and the utility of A-LORAKS-CS in achieving fast and automated reconstructions of undersampled multi-coil acquisitions.

4 Discussion

In this study, we introduced a hybrid PI-CS reconstruction, A-LORAKS-CS, with data-driven parameter tuning to improve practical utility. A-LORAKS-CS is a composite of LORAKS as its PI component, and sparsity-enforcing regularizations in wavelet- and TV-domains as its CS component. The primary parameters of interest for the proposed method are the rank of the system matrix in LORAKS, and weights of the regularization terms in wavelet and TV domains. A SURE expression is derived for the Hermitian symmetric LORAKS operator to construct the system matrix, and then used to identify the matrix rank via singular value thresholding. Meanwhile, the selection of the regularization weight in wavelet domain is based on online estimates of reconstruction error via a SURE expression, and the selection of the TV regularization weight is based on online estimates of local standard deviation in reconstructions. Taken together, these parameter selection strategies automate accelerated MRI reconstruction while alleviating the need for manual intervention. Our results strongly indicate that the proposed method performs reliably across different anatomies, sequences, and acceleration rates;

Table 2
Quality of in vivo bSSFP reconstructions in the brain assessed via PSNR, SSIM and NMSE. Measurements were averaged across cross-sections within each subject, and reported as mean ± std across subjects. Bold font marks the top performing reconstructions apart from the brute-force methods (marked in italic font).

PSNR (dB)

Acceleration	A-ESPIRiT	A-LORAKS	*BF-LORAKS*	PESCaT	**A-LORAKS-CS**	*BF-LORAKS-CS*
$R=2$	29.70 ± 1.17	**37.31 ± 0.47**	*37.31 ± 0.49*	34.49 ± 0.38	37.15 ± 0.52	*39.20 ± 0.35*
$R=3$	24.29 ± 0.67	32.53 ± 0.47	*32.57 ± 0.49*	30.54 ± 0.35	**33.40 ± 0.57**	*35.17 ± 0.46*
$R=4$	22.10 ± 2.08	30.61 ± 0.52	*30.83 ± 0.44*	28.78 ± 0.32	**31.46 ± 0.55**	*33.12 ± 0.39*

SSIM (%)

Acceleration	A-ESPIRiT	A-LORAKS	*BF-LORAKS*	PESCaT	**A-LORAKS-CS**	*BF-LORAKS-CS*
$R=2$	81.57 ± 4.04	94.84 ± 0.68	*94.86 ± 0.68*	94.29 ± 0.62	**96.39 ± 0.55**	*97.37 ± 0.26*
$R=3$	65.27 ± 3.51	87.56 ± 1.37	*87.67 ± 1.45*	89.08 ± 0.96	**93.22 ± 1.03**	*94.76 ± 0.48*
$R=4$	58.67 ± 7.87	83.85 ± 2.07	*83.97 ± 2.06*	85.82 ± 1.12	**90.81 ± 1.37**	*92.73 ± 0.56*

NMSE (10^{-2})

Acceleration	A-ESPIRiT	A-LORAKS	*BF-LORAKS*	PESCaT	**A-LORAKS-CS**	*BF-LORAKS-CS*
$R=2$	1.11 ± 0.36	**0.19 ± 0.03**	*0.19 ± 0.03*	0.36 ± 0.06	0.20 ± 0.04	*0.12 ± 0.02*
$R=3$	3.82 ± 0.87	0.56 ± 0.09	*0.55 ± 0.09*	0.88 ± 0.12	**0.47 ± 0.11**	*0.31 ± 0.05*
$R=4$	6.85 ± 3.39	0.87 ± 0.17	*0.83 ± 0.14*	1.32 ± 0.17	**0.73 ± 0.16**	*0.49 ± 0.07*

Table 3
Quality of in vivo T1-weighted brain reconstructions assessed via PSNR, SSIM and NMSE. Measurements were averaged across cross-sections within each subject, and reported as mean ± std across subjects. Bold font marks the top performing reconstructions apart from the brute-force methods (marked in italic font).

PSNR (dB)

Acceleration	A-ESPIRiT	A-LORAKS	*BF-LORAKS*	PESCaT	**A-LORAKS-CS**	*BF-LORAKS-CS*
$R=2$	29.24 ± 1.57	30.69 ± 1.27	*30.87 ± 1.40*	30.30 ± 1.02	**31.17 ± 1.22**	*32.42 ± 1.36*
$R=3$	24.79 ± 1.82	26.29 ± 1.27	*26.17 ± 1.61*	26.96 ± 0.99	**28.10 ± 1.22**	*28.71 ± 1.38*
$R=4$	22.14 ± 1.61	23.67 ± 1.37	*23.74 ± 1.28*	25.04 ± 0.99	**26.34 ± 1.32**	*26.11 ± 1.28*
$R=6$	17.56 ± 2.58	22.74 ± 1.16	*22.77 ± 1.17*	23.28 ± 1.01	**24.12 ± 1.27**	*24.33 ± 1.22*

SSIM (%)

Acceleration	A-ESPIRiT	A-LORAKS	*BF-LORAKS*	PESCaT	**A-LORAKS-CS**	*BF-LORAKS-CS*
$R=2$	89.56 ± 1.57	92.02 ± 0.97	*92.35 ± 1.11*	93.51 ± 0.43	**94.45 ± 0.48**	*95.31 ± 0.59*
$R=3$	78.09 ± 4.18	82.71 ± 1.68	*83.33 ± 2.10*	88.57 ± 0.46	**90.61 ± 0.62**	*91.37 ± 1.17*
$R=4$	68.56 ± 3.81	74.87 ± 2.40	*77.32 ± 2.27*	84.96 ± 0.35	**87.83 ± 0.68**	*87.51 ± 0.86*
$R=6$	58.91 ± 13.82	75.28 ± 1.98	*75.06 ± 2.34*	80.47 ± 0.40	**83.23 ± 0.67**	*83.88 ± 0.90*

NMSE (10^{-2})

Acceleration	A-ESPIRiT	A-LORAKS	*BF-LORAKS*	PESCaT	**A-LORAKS-CS**	*BF-LORAKS-CS*
$R=2$	0.50 ± 0.10	0.35 ± 0.04	*0.34 ± 0.05*	0.38 ± 0.04	**0.31 ± 0.04**	*0.24 ± 0.03*
$R=3$	1.42 ± 0.39	0.96 ± 0.12	*1.01 ± 0.25*	0.83 ± 0.10	**0.64 ± 0.09**	*0.56 ± 0.12*
$R=4$	2.57 ± 0.50	1.77 ± 0.27	*1.74 ± 0.22*	1.29 ± 0.17	**0.96 ± 0.17**	*1.01 ± 0.15*
$R=6$	8.08 ± 4.54	2.18 ± 0.21	*2.16 ± 0.22*	1.93 ± 0.28	**1.60 ± 0.27**	*1.52 ± 0.23*

and it maintains on par image quality to exhaustive parameter selection.

Several previous studies have demonstrated the use of SURE criterion for MRI reconstruction in order to select parameters for ESPIRiT, ℓ_1-norm regularization of wavelet coefficients, or TV regularization of image coefficients [32–34]. In particular, A-ESPIRiT uses a SURE expression to determine the optimal kernel size, subspace dimensionality and eigenvalue threshold [33]. Compared to A-ESPIRiT, A-LORAKS-CS should provide increased flexibility regarding

Table 4
Quality of in vivo TOF brain reconstructions assessed via PSNR, SSIM and NMSE. Measurements were averaged across cross-sections within each subject, and reported as mean ± std across subjects. Bold font marks the top performing reconstructions apart from the brute-force methods (marked in italic font).

PSNR (dB)

Acceleration	A-ESPIRiT	A-LORAKS	*BF-LORAKS*	PESCaT	**A-LORAKS-CS**	*BF-LORAKS-CS*
$R=2$	23.50 ± 2.37	23.81 ± 0.63	*24.15 ± 0.72*	27.21 ± 0.33	**29.30 ± 0.61**	*28.64 ± 0.75*
$R=3$	22.94 ± 2.55	20.78 ± 0.53	*20.69 ± 0.40*	23.66 ± 0.41	**26.12 ± 0.59**	*25.12 ± 0.65*
$R=4$	20.46 ± 1.95	19.48 ± 0.59	*19.91 ± 1.08*	21.18 ± 0.39	**24.08 ± 0.69**	*23.15 ± 0.86*

SSIM (%)

Acceleration	A-ESPIRiT	A-LORAKS	*BF-LORAKS*	PESCaT	**A-LORAKS-CS**	*BF-LORAKS-CS*
$R=2$	61.98 ± 7.33	63.19 ± 3.04	*68.12 ± 3.22*	81.62 ± 1.04	**86.31 ± 0.85**	*85.21 ± 0.88*
$R=3$	64.01 ± 9.55	50.25 ± 3.98	*55.36 ± 3.31*	70.92 ± 1.58	**78.37 ± 1.30**	*76.19 ± 1.34*
$R=4$	48.56 ± 6.78	44.43 ± 4.46	*49.42 ± 4.48*	62.39 ± 2.04	**72.16 ± 1.73**	*69.80 ± 2.47*

NMSE (10^{-2})

Acceleration	A-ESPIRiT	A-LORAKS	*BF-LORAKS*	PESCaT	**A-LORAKS-CS**	*BF-LORAKS-CS*
$R=2$	1.71 ± 1.04	1.44 ± 0.18	*1.33 ± 0.14*	0.66 ± 0.08	**0.41 ± 0.05**	*0.48 ± 0.08*
$R=3$	2.35 ± 2.30	2.88 ± 0.27	*2.99 ± 0.36*	1.49 ± 0.17	**0.85 ± 0.09**	*1.08 ± 0.16*
$R=4$	3.30 ± 1.48	3.88 ± 0.29	*3.58 ± 0.56*	2.65 ± 0.18	**1.37 ± 0.15**	*1.69 ± 0.20*

Table 5
Quality of in vivo FSE knee reconstructions assessed via PSNR, SSIM and NMSE. Measurements were averaged across cross-sections within each subject, and reported as mean ± std across subjects. Bold font marks the top performing reconstructions apart from the brute-force methods (marked in italic font).

PSNR (dB)

Acceleration	A-ESPIRiT	A-LORAKS	*BF-LORAKS*	PESCaT	**A-LORAKS-CS**	*BF-LORAKS-CS*
$R=2$	23.49 ± 0.45	26.32 ± 0.30	*29.23 ± 0.26*	**30.29 ± 0.27**	30.19 ± 0.26	*30.29 ± 0.19*
$R=3$	19.83 ± 0.93	22.59 ± 0.32	*27.19 ± 0.20*	28.13 ± 0.33	**28.27 ± 0.33**	*28.31 ± 0.30*
$R=4$	20.61 ± 2.73	21.82 ± 0.31	*26.19 ± 0.24*	27.03 ± 0.36	**27.29 ± 0.39**	*27.32 ± 0.30*

SSIM (%)

Acceleration	A-ESPIRiT	A-LORAKS	*BF-LORAKS*	PESCaT	**A-LORAKS-CS**	*BF-LORAKS-CS*
$R=2$	60.20 ± 2.82	74.16 ± 1.75	*84.55 ± 0.88*	85.98 ± 0.52	**86.26 ± 0.45**	*86.28 ± 0.48*
$R=3$	41.98 ± 4.44	56.90 ± 2.14	*76.31 ± 1.10*	77.80 ± 0.65	**78.59 ± 0.48**	*78.61 ± 0.64*
$R=4$	47.25 ± 14.41	52.63 ± 2.16	*71.02 ± 1.10*	72.40 ± 0.78	**73.49 ± 0.68**	*73.85 ± 0.76*

NMSE (10^{-2})

Acceleration	A-ESPIRiT	A-LORAKS	*BF-LORAKS*	PESCaT	**A-LORAKS-CS**	*BF-LORAKS-CS*
$R=2$	2.31 ± 0.25	1.20 ± 0.08	*0.61 ± 0.04*	**0.48 ± 0.03**	0.49 ± 0.03	*0.48 ± 0.03*
$R=3$	5.45 ± 1.32	2.82 ± 0.14	*0.98 ± 0.05*	0.79 ± 0.06	**0.76 ± 0.06**	*0.76 ± 0.06*
$R=4$	5.14 ± 2.78	3.35 ± 0.15	*1.23 ± 0.08*	1.02 ± 0.08	**0.96 ± 0.08**	*0.95 ± 0.06*

the design of sampling patterns, as the LORAKS framework can also operate in the absence of calibration regions. Furthermore, A-LORAKS-CS also devises parameter selection strategies for CS projections to further improve the reconstruction quality by alleviating the residual artifacts. Compared to the methods for wavelet-domain or TV-domain regularized reconstructions, A-LORAKS-CS incorporates a data-driven parameter selection for the PI component, and it employs a hybrid weight selection strategy for combined ℓ_1-TV-norm regularization. Compared to the PESCaT technique [29], our method incorporates a data-driven parameter selection for PI projections. Furthermore, while PES offers improved efficiency over standard line-search-based tuning methods, it still requires empirically tuned scaling factors for

epigraph sets and an iterative optimization for selection of TV weights.

Deep learning methods have recently been introduced that can learn regularization parameters to help automate MRI reconstructions. In particular, Hammernik et al. proposed a supervised reconstruction model that learns the reconstruction filters along with a regularization weight [46]. The supervised model is trained using a relatively large dataset of undersampled and corresponding fully-sampled acquisitions. The trained values of reconstruction and regularization parameters are then employed during inference without further updates. Since no parameter selection is performed during inference, learning-based methods offer significantly faster inference compared to iterative reconstruction methods. In contrast, the proposed method uses SURE-based estimators that involve line searches for relevant regularization parameters that will incur added computational costs. That said, the proposed method does not require large, paired training datasets that may be hard to compile. Furthermore, it performs scan-specific tuning of regularization parameters, permitting selection of a different regularization parameter for each subject. Future studies are warranted to comparatively examine the generalization performance learning-based versus iterative methods.

A limitation of the brute-force reconstructions is that they perform search over a restricted range of discrete parameter values due to computational considerations. While the implementation of brute-force methods used here has also been adopted in other studies [26,29], discrete sampling over a restricted range may lead to suboptimal performance. In turn, brute-force reconstructions may not be representative of the highest achievable image quality. Indeed, we have occasionally observed that the data-driven parameter-tuning techniques yield higher PSNR or SSIM values compared to brute-force methods (see Tables 1, 3 and 4). Nevertheless, brute-force methods still provide a target level for the attainable image quality in MRI reconstruction.

The proposed method can be advanced along several lines of technical development. Here, we used the soft-threshold heuristic approach for quasi-optimal albeit efficient selection of the system matrix rank in LORAKS under structured noise. Although nontrivial, a SURE-optimal derivation for rank selection is theoretically possible, and it might result in further performance gains. Second, the CS projections based on wavelet and TV domains were observed to perform well in brain and knee MRI reconstructions. Yet, they might be suboptimal for other MRI applications such as dynamic imaging where temporal sparsity might be an equally important factor [47]. Alternative domains can then be adopted to enforce compressibility of MR images during CS projections, and automated parameter selection strategies can be developed. Third, the SURE-estimators of online reconstruction error for matrix rank and wavelet threshold were utilized in conjunction with a line search. These linear searches can elevate computational load over methods with fixed parameters. When the computational cost of line searches become prohibitive, more efficient, direct selection approaches can be preferred [29,48]. Reconstructions can also be accelerated via parallelized implementations on central and/or graphics processing units.

In summary, we introduced a data-driven parameter selection approach to facilitate the reconstruction of multi-coil MRI datasets without the need for exhaustive hand-tuning of reconstruction parameters. The proposed approach was demonstrated to perform reliably for bSSFP, T_1-weighted, and TOF imaging of the brain, and PD-weighted FSE imaging of the knee. The presented results suggest great promise for advancing the clinical utility of hybrid PI-CS reconstructions.

Funding

This work was supported in part by a European Molecular Biology Organization Installation Grant (IG 3028), by a TUBA GEBIP 2015 fellowship, by a BAGEP 2017 fellowship, and by a TUBITAK 1001 Research Grant (117E171).

Declaration of interests

The authors declare that they have no known competing financial interests or personal relationships that could have appeared to influence the work reported in this paper.

Acknowledgements

In vivo knee data used in the preparation of this article were obtained from the Stanford fully-sampled 3D FSE knees database [44]. As such, investigators of this database provided data but did not participate in analysis or writing of this report. A listing of the knee database investigators can be found at http://mridata.org/.

Finally, authors would like to thank Toygan Kilic for his contributions to this work, and Tamara Danilyuk for her assistance in manuscript preparation.

Appendix A

The nonconvex penalty function $J_r(\cdot)$ in LORAKS enforces the rank of the system matrix to be less than or equal to r, and it is defined as follows:

$$J_r\left(P_S(x)\right) = \sum_{i>r} \varepsilon_i^2 \tag{18}$$

where the operator $P_S(\cdot)$ constructs the structured low-rank matrix S based on limited spatial support and/or smoothly varying phase from C-different receiver channels, and ε_i denotes the ith singular value of the matrix S. Minimizing

the loss function in Eq. (18) is equivalent to finding a rank-constrained approximation to S:

$$\min_x J_r\left(P_S\left(x\right)\right) = P_S^*\left(\underset{T:rank(T)\leq r}{\operatorname{argmin}} \|S-T\|_F^2\right) \tag{19}$$

where P_S^* is the adjoint of P_S that maps a structured matrix onto respective k-space data, T is the low-rank approximation to S, and $\|\cdot\|_F$ denotes Frobenius norm. Note that $P_S^*\left(P_S\left(x\right)\right)$ denotes a linear operator that maps each k-space sample onto itself, scaled by the number of times the sample appears in S. Therefore, $P_S^* P_S$ is a diagonal matrix with real entries.

Without loss of generality, the system matrix for a single receive-channel setup can be constructed as follows. Let $\tilde{\rho}\left(n_x, n_y\right)\left(n_x \in [-N_X, +N_X], n_y \in [-N_Y, +N_Y]\right)$ be Nyquist-sampled Cartesian k-space samples of a 2D image, where N_X and N_Y are positive integers that define the k-space measurement region. Then, let $S_c \in \mathbb{R}^{2K\times 2N_{NR}}$ be the structured matrix for the cth receiver channel. The operator $P_S\left(\cdot\right)$ constructs S_c by performing linear operations on k-space data $\tilde{\rho}\left(n_x, n_y\right)$. LORAKS employs a purely-real implementation for the matrix S_c that partitions real and imaginary components of the complex nullspace relationships:

$$S_c = \begin{bmatrix} S_{re+} - S_{re-} & -S_{im+} + S_{im-} \\ S_{im+} + S_{im-} & S_{re+} + S_{re-} \end{bmatrix} \tag{20}$$

The subblocks in S_c are defined based on real and imaginary components of k-space data in mirror-symmetric quadrants. Accordingly, $S_{re+}, S_{re-}, S_{im+}, S_{im-} \in \mathbb{R}^{K\times N_{NR}}$ are taken as:

$$\begin{aligned} \left[S_{re+}\right]_{k,m} &= \tilde{\rho}^{re}\left(n_x^{(k)} - p_m, n_y^{(k)} - q_m\right) \\ \left[S_{re-}\right]_{k,m} &= \tilde{\rho}^{re}\left(-n_x^{(k)} - p_m, -n_y^{(k)} - q_m\right) \\ \left[S_{im+}\right]_{k,m} &= \tilde{\rho}^{im}\left(n_x^{(k)} - p_m, n_y^{(k)} - q_m\right) \\ \left[S_{im-}\right]_{k,m} &= \tilde{\rho}^{im}\left(-n_x^{(k)} - p_m, -n_y^{(k)} - q_m\right) \end{aligned} \tag{21}$$

where $k = 1, \ldots, K$ and $m = 1, \ldots, N_{NR}$ and $\tilde{\rho}^{re}\left(n_x, n_y\right)$ and $\tilde{\rho}^{im}\left(n_x, n_y\right)$ denote the real and imaginary components of $\tilde{\rho}\left(n_x, n_y\right)$. Here K distinct k-space samples are indexed by $\left\{\left(n_x^{(k)}, n_y^{(k)}\right)\right\}_{k=1}^{K}$, and are chosen to be the full set of the k-space locations $\left(n_x, n_y\right)$ from the Cartesian grid that satisfy $-N_X + NR \leq n_x \leq N_X - NR$ and $-N_Y + NR \leq n_y \leq N_Y - NR$; $\{(p_m, q_m)\}_{m=1}^{N_{NR}}$ denotes the set of distinct elements from the set $\Lambda_{NR} = \left\{(p, q) \in \mathbb{Z}^2 : \left(p^2 + q^2 \leq NR^2\right)\right\}$, and N_{NR} is the number of elements on Λ_{NR}.

Finally, the LORAKS matrix S is constructed by concatenation of matrices across C-different receive channels:

$$S = [S_1, S_2, \ldots, S_C] \tag{22}$$

Appendix B Supplementary data

Supplementary data associated with this article can be found, in the online version, at https://doi.org/10.1016/j.zemedi.2022.02.002.

References

[1] Haldar JP, Zhuo J. P-LORAKS: low-rank modeling of local k-space neighborhoods with parallel imaging data. Magn Reson Med 2016;75:1499–514, http://dx.doi.org/10.1002/mrm.25717.

[2] Pruessmann KP, Weiger M, Scheidegger MB, Boesiger P. SENSE: sensitivity encoding for fast MRI. Magn Reson Med 1999;42:952–62.

[3] Griswold MA, Jakob PM, Heidemann RM, Nittka M, Jellus V, Wang J, et al. Generalized autocalibrating partially parallel acquisitions (GRAPPA). Magn Reson Med 2002;47:1202–10, http://dx.doi.org/10.1002/mrm.10171.

[4] Lustig M, Pauly JM. SPIRiT: iterative self-consistent parallel imaging reconstruction from arbitrary k-space. Magn Reson Med 2010;64:457–71, http://dx.doi.org/10.1002/mrm.22428.

[5] Haldar JP. Low-rank modeling of local k-space neighborhoods (LORAKS) for constrained MRI. IEEE Trans Med Imaging 2014;33:668–81, http://dx.doi.org/10.1109/TMI.2013.2293974.

[6] Zhang J, Liu C, Moseley ME. Parallel reconstruction using null operations. Magn Reson Med 2011;66:1241–53, http://dx.doi.org/10.1002/mrm.22899.

[7] Lustig M, Donoho D, Pauly JM. Sparse MRI: the application of compressed sensing for rapid MR imaging. Magn Reson Med 2007;58:1182–95, http://dx.doi.org/10.1002/mrm.21391.

[8] Çukur T, Lustig M, Nishimura DG. Improving non-contrast-enhanced steady-state free precession angiography with compressed sensing. Magn Reson Med 2009;61:1122–31, http://dx.doi.org/10.1002/mrm.21907.

[9] Jung H, Sung K, Nayak KS, Kim EY, Ye JC. k-t FOCUSS: a general compressed sensing framework for high resolution dynamic MRI. Magn Reson Med 2009;61:103–16.

[10] Bilgic B, Goyal VK, Adalsteinsson E. Multi-contrast reconstruction with Bayesian compressed sensing. Magn Reson Med 2011;66:1601–15.

[11] Ilicak E, Cetin S, Bulut E, Oguz KK, Saritas EU, Unal G, et al. Targeted vessel reconstruction in non-contrast-enhanced steady-state free precession angiography. NMR Biomed 2016;29:532–44, http://dx.doi.org/10.1002/nbm.3497.

[12] Hüfken T, Arbogast JM, Bracher AK, Beer M, Neubauer H, Rasche V. Accelerated model-based quantitative diffusion MRI: a feasibility study for musculoskeletal application. Z Med Phys 2021, http://dx.doi.org/10.1016/j.zemedi.2021.04.004.

[13] Uecker M, Lai P, Murphy MJ, Virtue P, Elad M, Pauly JM, et al. ESPIRiT – an eigenvalue approach to autocalibrating parallel MRI: where SENSE meets GRAPPA. Magn Reson Med 2014;71:990–1001, http://dx.doi.org/10.1002/mrm.24751.

[14] Murphy M, Alley M, Demmel J, Keutzer K, Vasanawala S, Lustig M. Fast ℓ_1-SPIRiT compressed sensing parallel imaging MRI: scalable parallel implementation and clinically feasible runtime. IEEE Trans Med Imaging 2012;31:1250–62, http://dx.doi.org/10.1109/TMI. 2012.2188039.

[15] Otazo R, Kim D, Axel L, Sodickson DK. Combination of compressed sensing and parallel imaging for highly accelerated

first-pass cardiac perfusion MRI. Magn Reson Med 2010;64:767–76, http://dx.doi.org/10.1002/mrm.22463.
[16] Hollingsworth KG. Reducing acquisition time in clinical MRI by data undersampling and compressed sensing reconstruction. Phys Med Biol 2015;60:R297–322, http://dx.doi.org/10.1088/0031-9155/60/21/R297.
[17] Lachner S, Utzschneider M, Zaric O, Minarikova L, Ruck L, Zbýň Š, et al. Compressed sensing and the use of phased array coils in 23Na MRI: a comparison of a SENSE-based and an individually combined multi-channel reconstruction. Z Med Phys 2021;31:48–57, http://dx.doi.org/10.1016/j.zemedi.2020.10.003.
[18] Haldar JP, Setsompop K. Linear predictability in magnetic resonance imaging reconstruction: leveraging shift-invariant Fourier structure for faster and better imaging. IEEE Signal Process Mag 2020;37:69–82, http://dx.doi.org/10.1109/MSP.2019.2949570.
[19] Haldar JP. LORAKS tech report; 2014. p. 1–21.
[20] Duan J, Liu C, Liu Y, Shang Z. Adaptive transform learning and joint sparsity based PLORAKS parallel magnetic resonance image reconstruction. IEEE Access 2020:212315–26, http://dx.doi.org/10.1109/ACCESS.2020.3039527.
[21] Bilgic B, Kim TH, Liao C, Manhard MK, Wald LL, Haldar JP, et al. Improving parallel imaging by jointly reconstructing multi-contrast data. Magn Reson Med 2018;80:619–32, http://dx.doi.org/10.1002/mrm.27076.
[22] Zhao B, Gagoski B, Adalsteinsson E, Grant PE, Wald LL. Accelerated HASTE-based fetal mri with low-rank modelling. In: Proc Int Soc Magn Reson Med, vol. 1. 2017. p. 4820.
[23] Lobos RA, Member S, Kim TH, Member S, Hoge WS, Haldar JP, et al. Navigator-free EPI ghost correction with structured low-rank matrix models: new theory and methods 2018;37:2390–402.
[24] Feng L, Benkert T, Block KT, Sodickson DK, Otazo R, Chandarana H. Compressed sensing for body MRI. J Magn Reson Imaging 2017;45:966–87, http://dx.doi.org/10.1002/jmri.25547.
[25] Jaspan ON, Fleysher R, Lipton ML. Compressed sensing MRI: a review of the clinical literature. Br J Radiol 2015;88:1–12, http://dx.doi.org/10.1259/bjr. 20150487.
[26] Akasaka T, Fujimoto K, Yamamoto T, Okada T, Fushumi Y, Yamamoto A, et al. Optimization of regularization parameters in compressed sensing of magnetic resonance angiography: can statistical image metrics mimic radiologists' perception? PLOS ONE 2016;11:1–14, http://dx.doi.org/10.1371/journal.pone.0146548.
[27] Zibetti MVW, Baboli R, Chang G, Otazo R, Regatte RR. Rapid compositional mapping of knee cartilage with compressed sensing MRI. J Magn Reson Imaging 2018, http://dx.doi.org/10.1002/jmri.26274.
[28] Lin F-H, Kwong KK, Belliveau JW, Wald LL. Parallel imaging reconstruction using automatic regularization. Magn Reson Med 2004;51:559–67, http://dx.doi.org/10.1002/mrm.10718.
[29] Shahdloo M, Ilicak E, Tofighi M, Saritas EU, Cetin AE, Cukur T. Projection onto epigraph sets for rapid self-tuning compressed sensing MRI. IEEE Trans Med Imaging 2019;38:1677–89.
[30] Sourbron S, Luypaert R, Van Schuerbeek P, Dujardin M, Stadnik T, Osteaux M. Deconvolution of dynamic contrast-enhanced MRI data by linear inversion: choice of the regularization parameter. Magn Reson Med 2004;52:209–13, http://dx.doi.org/10.1002/mrm.20113.
[31] Stein CM. Estimation of the mean of a multivariate normal distribution. Ann Stat 1981;9:1100–20, http://dx.doi.org/10.1214/aos/1176345632.
[32] Weller DS, Ramani S, Nielsen J-F, Fessler Ja. Monte Carlo SURE-based parameter selection for parallel magnetic resonance imaging reconstruction. Magn Reson Med 2014;71:1760–70, http://dx.doi.org/10.1002/mrm.24840.
[33] Iyer S, Ong F, Setsompop K, Doneva M, Lustig M. SURE-based automatic parameter selection for ESPIRiT calibration. Magn Reson Med 2020:1–15, http://dx.doi.org/10.1002/mrm.28386.
[34] Khare K, Hardy CJ, King KF, Turski PA, Marinelli L. Accelerated MR imaging using compressive sensing with no free parameters. Magn Reson Med 2012;68:1450–7, http://dx.doi.org/10.1002/mrm.24143.
[35] Ramani S, Weller DS, Nielsen JF, Fessler JA. Non-Cartesian MRI reconstruction with automatic regularization via Monte-Carlo SURE. IEEE Trans Med Imaging 2013;32:1411–22, http://dx.doi.org/10.1109/TMI.2013.2257829.
[36] Ilicak E, Çukur T. Parameter-free profile encoding reconstruction for multiple-acquisition bSSFP imaging. In: Proc Int Soc Magn Reson Med, vol. 25. 2017. p. 0571.
[37] Weingärtner S, Wetterling F, Konstandin S, Fatar M, Neumaier-Probst E, Schad LR. Scan time reduction in23Na-magnetic resonance imaging using the chemical shift imaging sequence: evaluation of an iterative reconstruction method. Z Med Phys 2015;25:275–86, http://dx.doi.org/10.1016/j.zemedi.2014.08.007.
[38] Kim TH, Haldar JP, Avenue M. USC-SIPI report # 443 LORAKS software version 2.0: faster implementation and enhanced capabilities by USC Viterbi School of Engineering Enhanced Capabilities; 2018, 0-24.
[39] Candes EJ, Sing-Long CA, Trzasko JD. Unbiased risk estimates for singular value thresholding and spectral estimators. IEEE Trans Signal Process 2013;61:4643–57, http://dx.doi.org/10.1109/TSP. 2013.2270464.
[40] Ilicak E, Senel LK, Biyik E, Çukur T. Profile-encoding reconstruction for multiple-acquisition balanced steady-state free precession imaging. Magn Reson Med 2017;78:1316–29, http://dx.doi.org/10.1002/mrm.26507.
[41] Selesnick IW, Bayram I. In: Total Variation Filtering [White Paper]; 2010.
[42] Guo W, Huang F. Adaptive total variation based filtering for MRI images with spatially inhomogeneous noise and artifacts. In: Proc - 2009 IEEE Int Symp Biomed Imaging from Nano to Macro, ISBI, 2009. 2009. p. 101–4, http://dx.doi.org/10.1109/ISBI. 2009.5192993.
[43] Çukur T, Lustig M, Saritas EU, Nishimura DG. Signal compensation and compressed sensing for magnetization-prepared MR angiography. IEEE Trans Med Imaging 2011;34:107–15.
[44] Epperson K, Rt R, Sawyer AM, Rt R, Lustig M, Alley M, et al. Creation of fully sampled MR data repository for compressed sensing of the knee. In: SMRT Conf, 2013. 2013. p. 1.
[45] Kroon DJ. Region growing. MATLAB central file exchange; 2021.
[46] Hammernik K, Klatzer T, Kobler E, Recht MP, Sodickson DK, Pock T, et al. Learning a variational network for reconstruction of accelerated MRI data. Magn Reson Med 2018;79:3055–71, http://dx.doi.org/10.1002/mrm.26977.
[47] Otazo R, Candès E, Sodickson DK. Low-rank plus sparse matrix decomposition for accelerated dynamic MRI with separation of background and dynamic components. Magn Reson Med 2015;73:1125–36, http://dx.doi.org/10.1002/mrm.25240.
[48] Varela-Mattatall G, Baron CA, Menon RS. Automatic determination of the regularization weighting for wavelet-based compressed sensing MRI reconstructions. Magn Reson Med 2021;86:1403–19, http://dx.doi.org/10.1002/mrm.28812.

Available online at www.sciencedirect.com
ScienceDirect